NJC

ROYAL SOCIETY OF CHEMISTRY

PAPER

View Article Online
View Journal | View Issue

Cite this: *New J. Chem.*, 2025, 49, 234

UV-assisted synthesis of an Ag-poly (aminosalicylic acid) hybrid system for an asymmetric supercapacitor and its application as a low pass filter†

Pooja Kumari,[a] Chandan Saha,[a] Sarit K Ghosh,[a] Venkata K Perla,[b] Harishchandra Singh[c] and Kaushik Mallick *[a]

Supercapacitors have attracted substantial research interest as energy storage devices because of their long cycle life, quick electrochemical charging–discharging process and high energy and power densities. In this study, a UV-light mediated synthesis route was applied to fabricate a silver-polymer (poly-aminosalicylic acid) [Ag-PASA] hybrid system as a cathode material for the preparation of an asymmetric supercapacitor. In a three-electrode setup, Ag-PASA as an active material displayed a specific capacity of 317 C g^{-1} at 5 mV s^{-1} in the presence of KOH (1 mol dm^{-3}) as an electrolyte. The assembled asymmetric device fabricated using Ag-PASA as a cathode material and activated carbon as an anode material exhibited a faradaic charge storage mechanism, achieving a specific capacity of 55 C g^{-1} at 5 mV s^{-1} and a capacity retention of 85% after 10^4 charge–discharge cycles at 1.4 A g^{-1}. The device delivered specific energy values of 9 and 15.1 W h kg^{-1} at specific powers of 1625 and 325 W kg^{-1}, respectively. Electrochemical results indicate that Ag-PASA could be an excellent cathode material for asymmetric supercapacitor applications. The fabricated supercapacitor was applied in an RC circuit to analyse its frequency response through both experimental and simulation methods. The results demonstrated an effective attenuation of high-frequency components, confirming a cut-off frequency of 3 Hz, which is critical for low pass filter application in audio processing and signal conditioning.

Received 27th October 2024,
Accepted 21st November 2024

DOI: 10.1039/d4nj04659e

rsc.li/njc

Introduction

In recent decades, researchers have increasingly focused on synthesizing nanomaterials with multiple functionalities.[1] Nanostructured materials exhibit excellent mechanical, optical, magnetic, catalytic and electrical behaviours that are significantly distinct from those of their bulk counterparts.[2] The characteristics of nanomaterials can be modified by controlling their size and shape through modifications of synthesis conditions and functionalization. Nanostructured silver particles are the most fascinating nanomaterials with a wide range of applications in catalysis,[3] sensing,[4] optics,[5] photonics,[6] biomedicine,[7] electronics,[8] energy storage,[9–12] and other fields.

Among the various energy storage materials,[13–17] electrochemical capacitors, also known as supercapacitors, have attracted significant attention as a storage device because of their high charge–discharge rate, long cycle life and high power and energy density.[1,18] Several reports have been published detailing the development and performance of silver nanoparticle-based materials specifically manufactured for supercapacitor applications. A silver nanoparticle decorated hybrid system of polyaniline (PANI)-reduced graphene oxide exhibited a specific capacitance (SC) of 385.4 F g^{-1} at 5 mV s^{-1}.[19] The nanocomposite of Ag-PANI-graphene on a carbon fiber electrode showed an SC value of 828 F g^{-1} at 1.5 A g^{-1} with a capacity retention of 97.5% after 3000 charge–discharge cycles.[20] It was reported that the Ag-PANI hybrid system displayed an SC value of 553 F g^{-1} at 1 A g^{-1}.[21] A silver nanoparticle decorated PANI-multiwall carbon nanotube-based electrode was applied for high-performance supercapacitor application, showing an SC of 862 F g^{-1}.[22] Silver-activated carbon-PANI-based hybrid system, deposited on stainless steel as a current collector, exhibited an SC value of 567 F g^{-1} at 5 mV s^{-1} owing to the synergistic interaction, where silver nanoparticles improved the electrical conductivity and activated carbon enhanced the electrochemical stability of the PANI-based electrode.[23]

[a] *Department of Chemical Sciences, University of Johannesburg, P.O. Box: 524, Auckland Park, 2006, South Africa. E-mail: kaushikm@uj.ac.za*
[b] *Laboratory of Organic Electronics, Department of Science and Technology, Linköping University, Norrköping, Sweden*
[c] *Nano and Molecular Systems Research Unit, University of Oulu, FIN-90014, Finland*

† Electronic supplementary information (ESI) available. See DOI: https://doi.org/10.1039/d4nj04659e

An electrode based on the PANI-cellulose supported silver nanoparticles displayed an SC value of 217 F g^{-1} with a capacitance retention of 83% after 1000 cycles.[24] The supercapacitive behavior of the Ag-PANI-carbon nitride-based electrode produced an SC of 797.8 F g^{-1} with a capacitance retention of 84.43% after 1000 cycles at 1 A g^{-1}.[25]

In this work, a poly-aminosalicylic acid stabilized silver nanoparticle-based hybrid system was synthesized using the UV-irradiation technique. The polymeric form of aminosalicylic acid, an analogous structure of polyaniline, is generally considered the most promising conducting polymer with multiple redox states, excellent environmental stability and low cost.[18] The hybrid system was applied as an active material for supercapacitor application for three-electrode and two-electrode coin cell-based devices. The silver nanoparticle was selected as the conductive dopant because silver is less expensive than other noble metals and also exhibits higher operation stability in comparison to conjugated polymers.[26] Silver nanoparticles can be synthesized using various methods, such as chemical reduction, pyrolysis, biosynthesis, and microbiological and physical processes.[27] Electric energy,[28] microwave energy,[29] radioactive energy[30] and light energy[31] are common physical methods used for synthesizing silver nanoparticles. Each method has several benefits and limitations, and the choice of method can depend on factors such as the desired size, shape and purity of the nanoparticles, as well as the specific application for which they are intended. UV light-mediated synthesis is less hazardous and provides precise control over the size and shape of nanoparticles by influencing the rate of nucleation and growth. This method operates in the absence of additional reducing agents, which helps in obtaining high-purity nanoparticles.

Experimental section

Material

The study utilized analytical grade 4-amino salicylic acid, silver nitrate, potassium hydroxide, *N*-methyl pyrrolidine (NMP) and poly-vinylidene fluoride (PVDF) without additional purification.

Synthesis of poly-amino salicylic acid stabilized silver nanoparticles

For a typical synthesis method, 0.250 g of 4-amino salicylic acid was dissolved in 10 mL of methanol in a conical flask. To this solution, 5 mL aqueous silver nitrate (1×10^{-2} mol dm^{-3}) was added dropwise with the formation of white-coloured Ag(I)-amino salicylic acid complex in the form of a precipitate. The complex material, under ultraviolet light irradiation, gradually changed its colour from white to brown, implying the formation of an Ag(0)-poly-aminosalicylic acid (Ag-PASA) hybrid system (Scheme 1). The synthesized material was filtered, dried under vacuum at 80 °C and ground to obtain the powder form.

The synthesized hybrid product was characterized using optical, microscopic and surface analytical techniques and

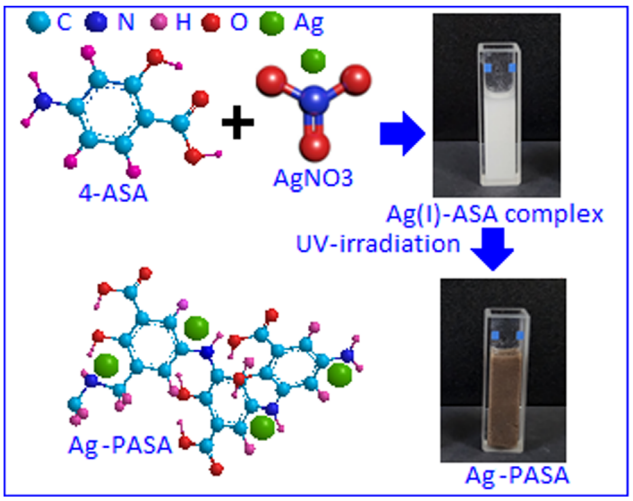

Scheme 1 Schematic of the formation of an Ag(0)-poly-aminosalicylic acid (Ag-PASA) hybrid system.

was also applied for supercapacitor application, demonstrating its potential for energy storage performance.

For a control experiment, poly-amino salicylic acid (PASA) was prepared using 4-amino salicylic acid (ASA) in the presence of ammonium persulphate as an oxidizing agent.

Electrode preparation and asymmetric supercapacitor device fabrication techniques are available in the ESI† section. Equations for electrochemical parameter evaluation are also available in the ESI† section.

Material characterization

The formation of nanoparticles was monitored spectroscopically using a UV-vis spectrophotometer (Shimadzu UV-1800). The X-ray diffraction pattern of the synthesized material was investigated using a Philips PANalytical X'pert diffractometer with Cu-Kα radiation and studied at an operating voltage of 40 kV in a diffraction angle range (2θ) of 25°–90°. A microscopy study was performed using a JEOL (JEM-2100) transmission electron microscope (TEM). The chemical composition and the oxidation state of the product were analysed using the X-ray photoelectron spectroscopy (XPS, Thermo Scientific MultiLab 2000) technique. The Raman spectrum (Jobin-Yvon T64000 Raman spectrometer) was acquired using 514.5 nm of an argon ion laser as the excitation source.

Results and discussion

The mechanism of the formation of the hybrid system can be explained as follows. In the presence of visible light, the reaction between amino salicylic acid and silver nitrate is a slow polymerization process *via* the formation of the Ag(I)-amino salicylic acid complex. This complex is a high band gap material, where electrons cannot easily cross the valence band barrier of the organic component. In the presence of UV-irradiation, the valence band electron of the organic material is transferred to the conduction band due to the decrease in band gap and expedites the

polymerization (oxidation) of amino salicylic acid with the formation of poly amino salicylic acid. The conduction band electron reduced the silver ion with the formation of silver atoms. The agglomeration of atoms ultimately formed nanosilver particles, which were stabilized by the polymer through functionalization.

The formation of silver nanoparticles was monitored spectroscopically using a UV-vis spectrophotometer. Silver nanoparticles absorb electromagnetic radiation in the range of 380–450 nm through a phenomenon known as the excitation of localized surface plasmon resonance.[32,33] Fig. 1 illustrates the optical response during the reaction between amino salicylic acid and silver nitrate under UV irradiation.

As the reaction progressed, there was a gradual increase in the intensity of the absorbance band at 405 nm, which served as a clear indicator of silver nanoparticle formation.[34] The increase in absorbance intensity over time suggests the successful synthesis of the nanoparticles and their growth as the reaction continues. This behavior indicates a dynamic process in which the silver ions are reduced into atoms and consequently aggregate to form nanoparticles.

The transmission electron microscopy image illustrated in Fig. 2A provides a detailed visualization of the synthesized silver-polymer hybrid system. The dark spots observed in the image correspond to silver particles in the range of 12–26 nm, as depicted in the histogram (Fig. 2B) and are uniformly distributed throughout the surrounding organic matrix. Additionally, the magnified TEM image depicted in Fig. 2C reveals the presence of smaller particles (marked by an arrow), typically measuring between 1 and 3 nm, which are not represented in the histogram. The UV light influences the formation of the nucleation centre of silver nanoparticles. The growth of the particles and their respective sizes depend on the UV-irradiation time.

The crystal structure of the synthesized silver particles was identified by applying an X-ray diffraction technique in the range (2θ) of 25–90° corresponding to ICDD: 04-002-1347[35] (Fig. 3A). The XRD pattern exhibits distinct diffraction peaks at angles of 2θ = 38.3°, 44.5°, 64.7°, 77.3° and 81.6°, which correspond to (111), (200), (220), (311) and (222) planes, respectively, for face-centered cubic silver atom. The additional diffraction peaks observed around 30° (marked within a circle) can be assigned to the polymeric form of aminosalicylic acid.

In the Raman spectrum (Fig. 3B), the different vibrational bands between 1100 and 1700 cm^{-1} are sensitive to the oxidation state of poly-aminosalicylic acid, which is the same as that of the polyaniline network. The benzene C–H bending deformation band positioned at 1160 cm^{-1} is a characteristic of semiquinone structures.[36] Two prominent vibration bands at 1205 and 1240 cm^{-1} correspond to the C–N stretching modes. An intense overlapping feature between 1300 and 1400 cm^{-1} corresponds to the C–N stretching vibration of the delocalized polaronic charge carriers and the area confirms the presence of

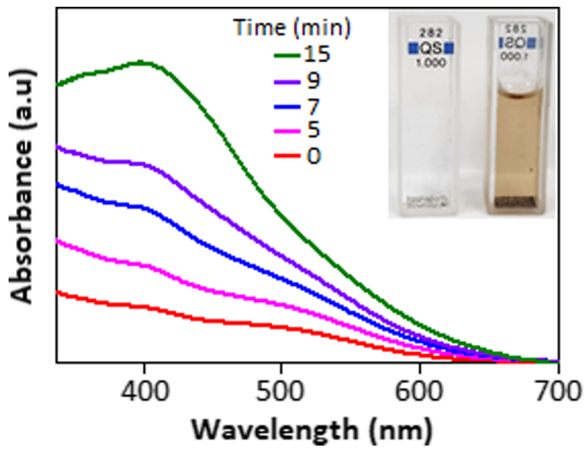

Fig. 1 UV-vis spectra of silver nanoparticles at different time intervals.

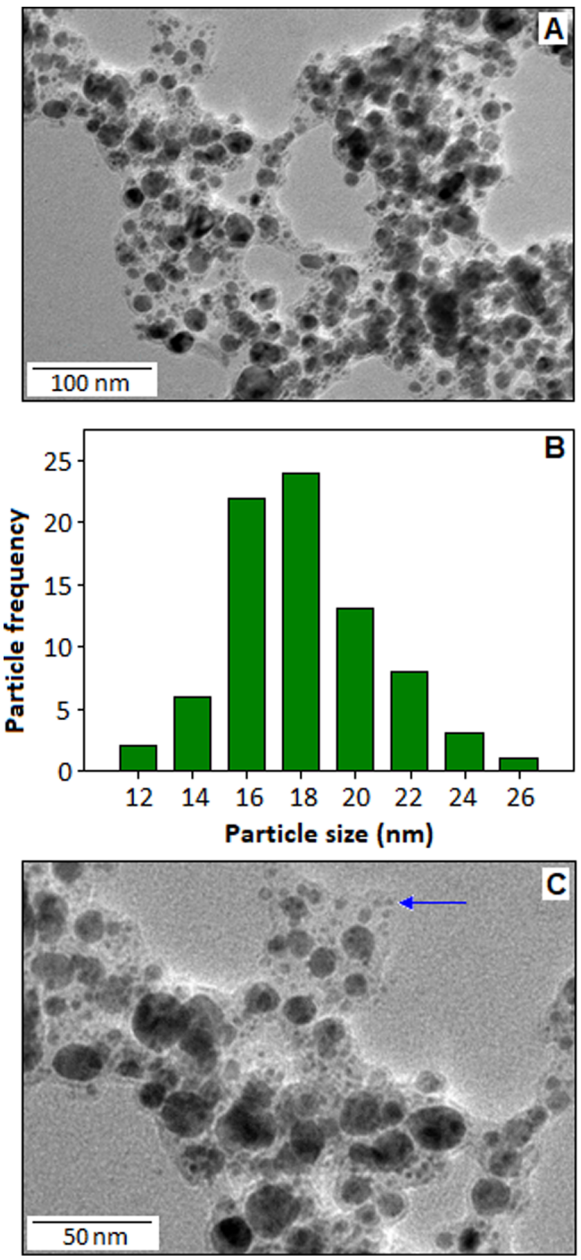

Fig. 2 (A) TEM image of the polymer-stabilized silver nanoparticles and the corresponding histogram (B). (C) Higher magnification TEM image.

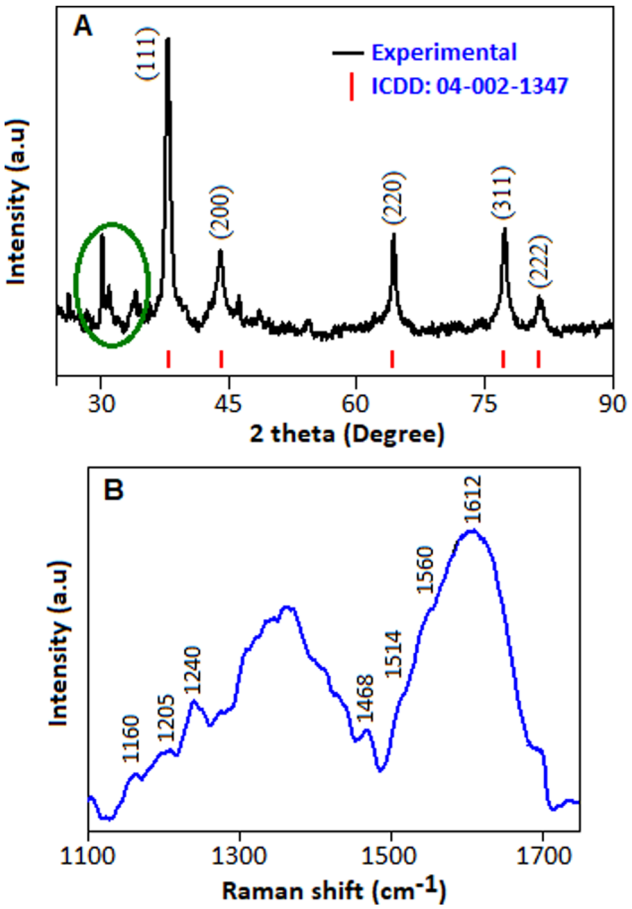

Fig. 3 (A) XRD pattern of Ag-poly-aminosalicylic. (B) Raman spectra of Ag-poly-aminosalicylic acid measured within the range of 1100–1700 cm^{-1}.

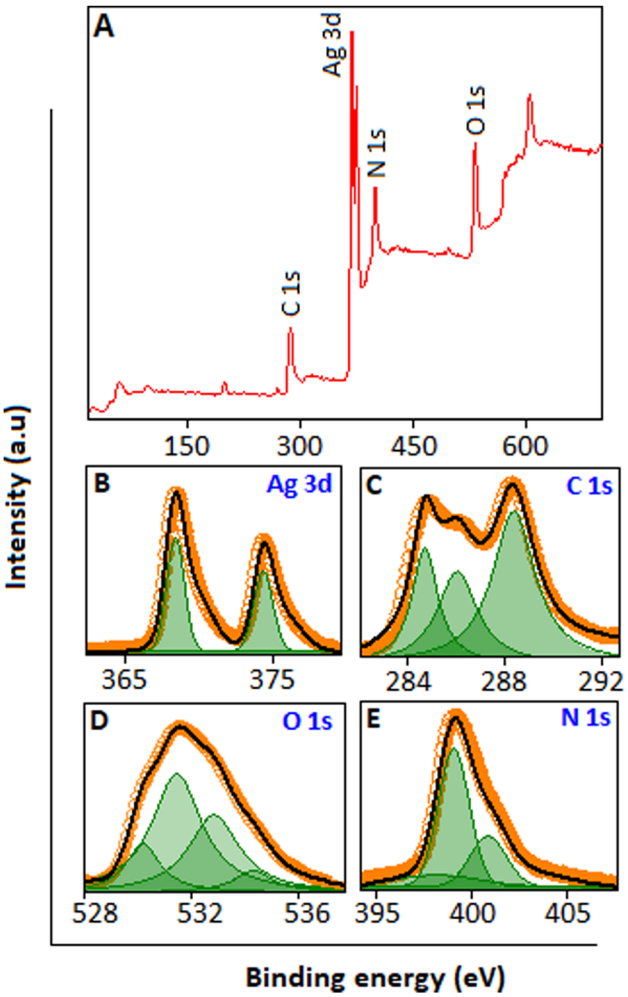

Fig. 4 (A) XPS survey spectrum of Ag-poly-aminosalicylic (main panel). High-resolution XPS spectrum of (B) Ag 3d, (C) C 1s, (D) O 1s and (E) N 1s.

a high concentration of these modes.[36] The band at 1468 cm^{-1} corresponds to the C═N stretching mode of the quinoid units. Another overlapping feature between 1500 cm^{-1} and 1650 cm^{-1} can be assigned to the C–C deformation bands of benzenoid rings, which are characteristic of the semiquinone structure.[37]

The elemental composition and the oxidation state of the silver-polymer hybrid system were investigated by applying an X-ray photoelectron spectroscopy (XPS) technique. Fig. 4A shows the survey spectrum with the elemental peaks of Ag, C, O and N. The high-resolution Ag 3d XPS spectrum (Fig. 4B) with peak values of 368 and 374 eV is attributed to Ag $3d_{5/2}$ and Ag $3d_{3/2}$, respectively, corresponding to the presence of metallic silver in the silver-polymer network.[38] Deconvoluted C 1s spectrum (Fig. 4C) shows three peaks with binding energies values of 284.6, 285.9 and 288.9 eV, corresponding to C–C, C–O and –COOH, respectively. The high-resolution O 1s spectrum (Fig. 4D) exhibits peaks at the binding energy values of 530, 531, 532 and 533 eV, which correspond with C–O, O–C═O, C═O and –COOH functionalities, respectively.[39] Deconvoluted high-resolution N 1s spectrum (Fig. 4E) displays quinonoid imine (═N–), benzenoid amine (–NH–) and positively charged nitrogen atoms ($–N^+$) at the binding energy values of 398.2, 399.4 and 400.2 eV, respectively.[40]

Supercapacitor performance

Three-electrode system. The electrochemical characteristics of the PASA- and Ag-PASA-modified Ni-foams as working electrodes were tested using the cyclic voltammetry (CV) technique. Fig. 5A displays the current response in the CV profiles of PASA and Ag-PASA under a scan rate of 20 mV s^{-1} in a KOH (1 mol dm^{-3}) solution.

The specific capacity (S_{CP}) of Ag-PASA was obtained as 230 C g^{-1} at 20 mV s^{-1}, which is much higher than the S_{CP} value of PASA (33 C g^{-1} at 20 mV s^{-1}), indicating a better charge storage capability. This improvement is reflected in the CV profiles, where Ag-PASA exhibits a larger integral area, signifying a higher energy storage capacity. The incorporation of silver nanoparticles into a polymer matrix enhances the electrical conductivity and hence the electrochemical behavior by increasing the number of redox-active sites along with the electrochemical surface area. These additional sites allow for efficient charge transfer and faster ion diffusion, resulting in improved redox kinetics. These factors led to the selection of Ag-PASA as the preferred electrode material for further studies.

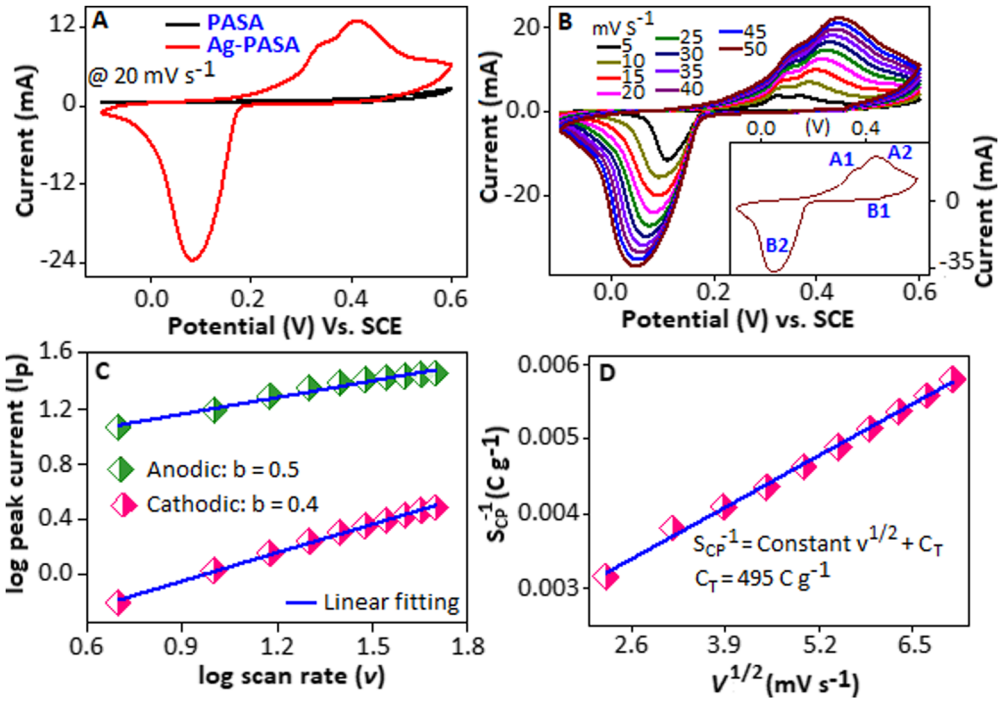

Fig. 5 (A) Cyclic voltammogram of poly-aminosalicylic acid and Ag-poly-aminosalicylic acid at a scan rate of 20 mV s^{-1} in the presence of KOH (1 mol dm^{-3}) as an electrolyte. (B) Cyclic voltammogram of Ag-poly-aminosalicylic acid under scan rates ranging from 5 to 50 mV s^{-1}. Inset figure shows the voltammogram at 50 mV s^{-1} with various redox peaks. (C) Graphical representation of peak current (I_p) as a function of the scan rate (v) in log–log scale. (D) Graphical representation of specific capacity (S_{CP}^{-1}) as a function of the scan rate ($v^{1/2}$).

The cyclic voltammograms of the Ag-PASA nanocomposite, recorded between 5 and 50 mV s^{-1}, revealed excellent redox characteristics and battery-like behaviour (Fig. 5B). The anodic curve displays two distinct oxidation peaks in the range of 0.25–0.38 V (A1), representing the oxidation of Ag to Ag_2O and at 0.44 V (A2) representing further oxidation of Ag_2O to AgO. In the cathodic curve, two peaks (B1 and B2) represent the reduction of AgO to Ag_2O and Ag_2O to Ag, respectively[41] (Fig. 5B, inset). The following reactions are responsible for the redox peaks in the CV profile:

$$Ag^0 + OH^- \leftrightarrow \tfrac{1}{2} Ag_2O + \tfrac{1}{2} H_2O + e^-$$

$$\tfrac{1}{2} Ag_2O + OH^- \leftrightarrow AgO + \tfrac{1}{2} H_2O + e^-.$$

The large area under the CV curve (Fig. 5B) indicates the quasi-reversible reaction mechanism of the material due to the faradaic reaction involving the transfer of two electrons. In the voltammogram, a large voltage difference between the cathodic and anodic peaks signifies the kinetic irreversibility of the reduction and oxidation processes. The oxidation and reduction peaks shifted to positive and negative potentials, respectively, at scan rates ranging from 5 to 50 mV s^{-1}, which signifies the quasi-reversibility of the material. This phenomenon is caused by ohmic resistance, slow electron transfer kinetics and low ionic diffusivity of the battery-type material.[42] The high conductivity of Ag facilitates faster electron transfer during redox reactions, improving the kinetics of charge storage and release processes. During the forward scan, the Ag-PASA-modified electrode was oxidized by ejecting the electron, leaving the material with unbalanced charges, which corresponds to the anodic peak ($Ag^0 \rightarrow Ag^{2+}$) at a potential ranging from 0.25 to 0.60 V for all scan rates. To maintain charge neutrality, OH^- ions are diffused from the bulk electrolyte solution into the Ag-PASA electrode. The process was reversed (reduction process) during the backward scan, and the cathodic peak ($Ag^{2+} \rightarrow Ag^0$) was observed at the potential ranging from 0.48 to −0.02 V for all the scan rates. The above observation indicates that the Ag-PASA electrode behaves as a battery-type electrode.[43] The S_{CP} of the Ag-PASA electrode was estimated from the CV curves (eqn (S1), ESI†) with values of 173 C g^{-1} at 50 mV s^{-1} and 317 C g^{-1} at 5 mV s^{-1}.

The charge storage behaviour of the Ag-PASA-based electrode was calculated using the power law equation: $I_p = av^b$ or $\log I_p = \log(a) + (b)\log v$ where I_p represents peak current, a and b are constants and v is the scan rate. The slope of the straight line determines the 'b' value, which can be 0.5 for a diffusion-controlled (C_D) process or 1 for a surface-controlled process (C_S).[44] In this study, the slopes of the anodic and cathodic peak currents were obtained as 0.5 and 0.4, respectively (Fig. 5C), signifying that the diffusion-controlled process is predominant for the charge storage mechanism. The C_D and C_S contributions were determined from CV data under the scan rate range of 5–50 mV s^{-1}, applying the Trasatti method.[45] The total specific capacity (C_T) was calculated based on the following equation: S_{CP}^{-1} = constant $v^{1/2} + C_T^{-1}$. Plotting the inverse of specific capacity (S_{CP}^{-1}) *vs.* ($v^{1/2}$) yielded a C_T value of 495 C g^{-1} (Fig. 5D). The surface contribution (C_S) was calculated using the following equation:

S_{CP} = constant $v^{1/2}$ + C_S. The intercept of the plot, S_{CP} *vs.* $v^{-1/2}$, yielded a C_S value of 117 C g^{-1} (Fig. 6A). Thus, the diffusion contribution (C_D) to the C_T can be calculated as follows: C_D = C_T − C_S.[46] The C_S and C_D contributions to the C_T of Ag-PASA-based electrode were 24 and 76%, respectively (Fig. 6B). In Fig. 6C, the plot of $I_p v^{-1/2}$ *vs.* $v^{1/2}$ was used to extract diffusion and surface-controlled contributions using Dunn's method[44] based on the following equations: $I_p = k_1 v + k_1 v^{1/2} = C_S + C_D$, which can be expressed as follows: $I_p/v^{1/2} = k_1 v^{1/2} + k_2$, where k_1 and k_2 are constants.

The percentage contributions of diffusion and surface-controlled charge storage for scan rates ranging from 5 to 50 mV s^{-1} are depicted in Fig. 6D.

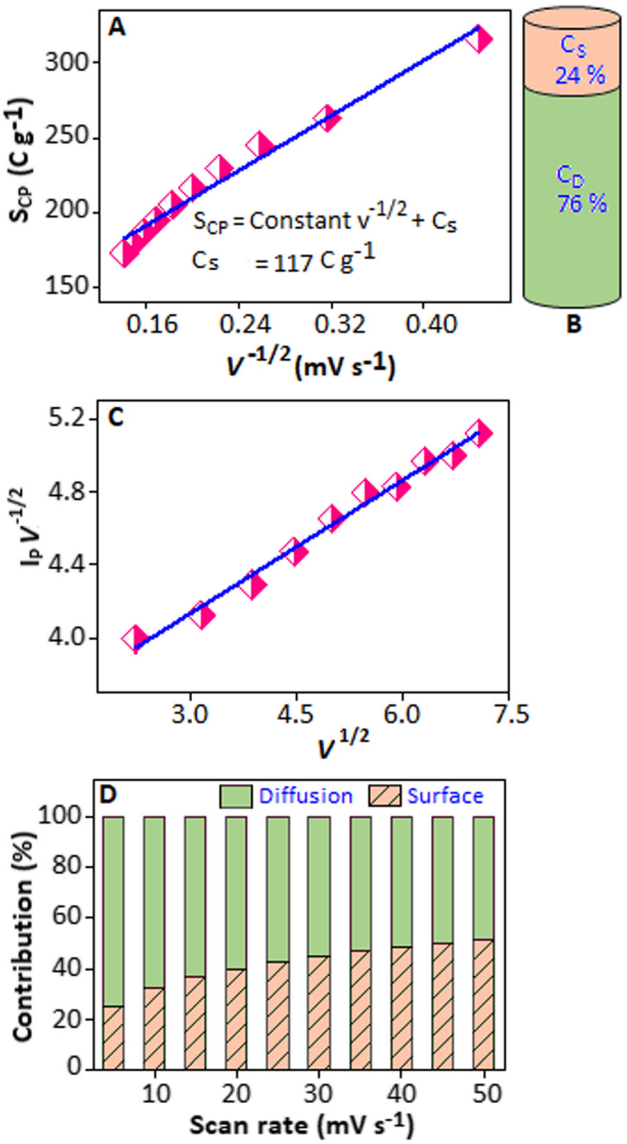

Fig. 6 (A) Graphical representation of specific capacity (S_{CP}) as a function of the scan rate ($v^{-1/2}$). (B) Charge storage contribution of the Ag-poly-aminosalicylic acid electrode, diffusion-controlled (C_D) and surface-controlled (C_S). (C) Plot of $I_p v^{-1/2}$ *vs.* $v^{1/2}$ used for calculating the constants of k_1 and k_2. (D) Diffusion and surface contribution (%) of the charge under various scan rates (5–50 mV s^{-1}).

Galvanostatic charge–discharge measurements were conducted to determine the specific capacity of the Ag-PASA electrode at different specific currents (16.0–3.0 A g^{-1}) ranging from −0.1 to 0.6 V, Fig. 7A. The S_{CP} values obtained as 214 C g^{-1} at 3 A g^{-1} and 134 C g^{-1} at 16 A g^{-1} were calculated using eqn (S2) (ESI†). The decrease in S_{CP} values with increasing current density or scan rate can be attributed to the following factors, such as insufficient penetration of electrolyte ions into the electrode material and increased charge transfer resistance. At higher current densities, the ions have less time to diffuse to the electrode surface, leading to incomplete charge–discharge processes that cause lower capacity values.

According to the literature, incorporating silver nanoparticles into both organic and inorganic matrices significantly enhances the charge storage capacity of the hybrid system. This enhancement occurs due to the unique properties of silver nanoparticles, which can improve electrical characteristics and facilitate better charge distribution within the matrix. Silver nanoparticles on PANI-multiwalled carbon nanotube-based hybrid system showed an SC of 528 F g^{-1} at 5 mV s^{-1}.[47] Polyaniline supported silver particles, with 0.9 wt% doping concentration of silver, on stainless steel electrode showed an SC of 512 F g^{-1} at 5 mV s^{-1}.[48] The supercapacitive behaviour of the polypyrrole-polyacrylic acid-silver nanocomposite-based electrodes showed an SC of 226 F g^{-1} at 10 mV s^{-1}.[49] It is reported that silver–manganese oxide hybrid material as a positive electrode demonstrated an SC of 154 F g^{-1} at 1 A g^{-1}.[1] The charge–discharge curves exhibit a sudden voltage drop, known as the IR drop, which occurs when the supercapacitor switches from charging to discharging process. This drop results from the combined ohmic resistance of the electrodes, electrolyte and contact resistances within the system, while a broad voltage plateau represents the quasi-faradaic process.[50,51] The discharge curve reveals a sudden potential increase from 0.14 to 0.19 V, marked within a circle, attributed to the quasi-reversible reaction mechanism.[52] The stability of the electrode was further studied for 3000 continuous charge–discharge cycles at 14 A g^{-1} and showed a capacity retention of 92% (Fig. 7A, inset). A comparable capacitance retention value has also been reported for silver-based nanocomposite systems. A hybrid system made with graphene, polypyrrole and silver nanoparticles, synthesized by *in situ* oxidative polymerization of pyrrole, exhibited an SC of 450 F g^{-1} at 0.9 mA g^{-1} and retained 92% of its initial value after 1000 charge–discharge cycles.[53] Screen-printed activated carbon–silver nanocomposite-based electrode showed an SC of 194 F g^{-1} with 89% of capacitance retention after 1000 cycles.[54]

The impedance characteristics of the Ag-PASA electrode were studied in the range of 10 mHz–100 kHz, which is linked to ion diffusion at the electrode–electrolyte interface. Fig. 7B (main panel) displays the fitted Nyquist plot with a quasi-semicircle in the high-frequency region and an inclined straight line in the low-frequency region. The magnified images of the Nyquist plot for the high-frequency region and the Randle circuit are displayed in Fig. 7B, insets (I) and (II), respectively.

This circuit consists of a solution resistance (R_s), which represents the resistance of the electrolyte between the counter

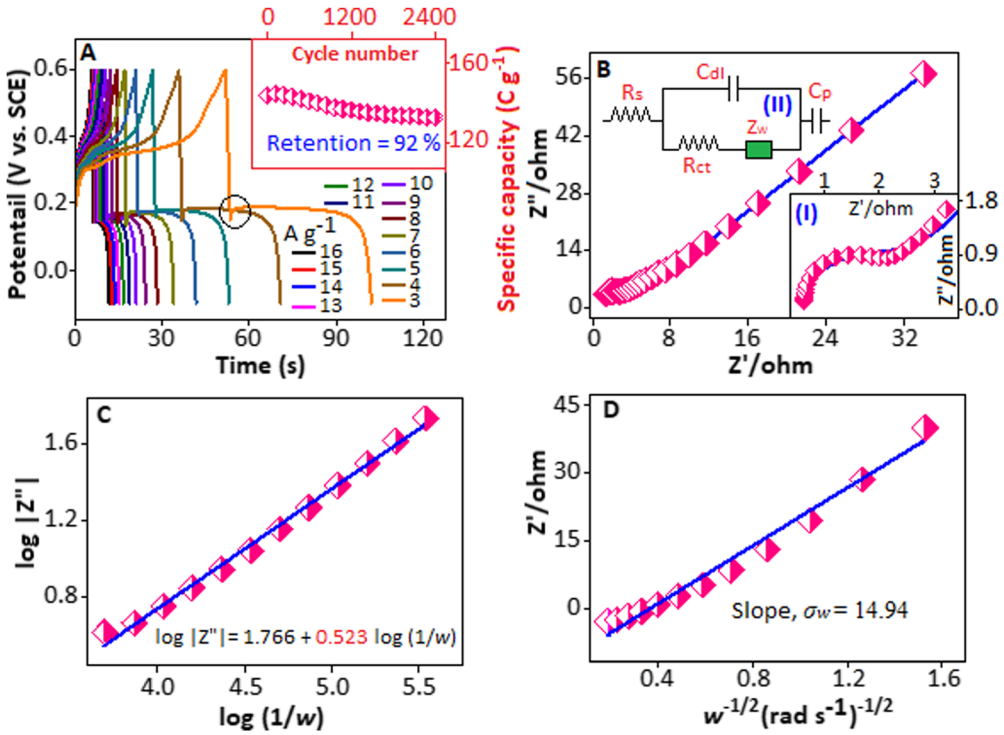

Fig. 7 (A) Galvanostatic charge discharge curves of the Ag-poly-aminosalicylic acid-based electrode under a specific current from 3.0 to 16.0 A g^{-1}. Inset figure represents capacity retention after 3000 charge–discharge cycles. (B) Nyquist plot of the electrode at frequencies ranging from 10 mHz to 100 kHz, inset figure (I) shows a magnified image of the Nyquist plot for the high-frequency region, and inset figure (II) shows the equivalent circuit model. (C) Plot of log|Z''| *vs.* log(1/ω) (D) Plot of Z' *vs.* $\omega^{-1/2}$ (rad s^{-1})$^{-1/2}$.

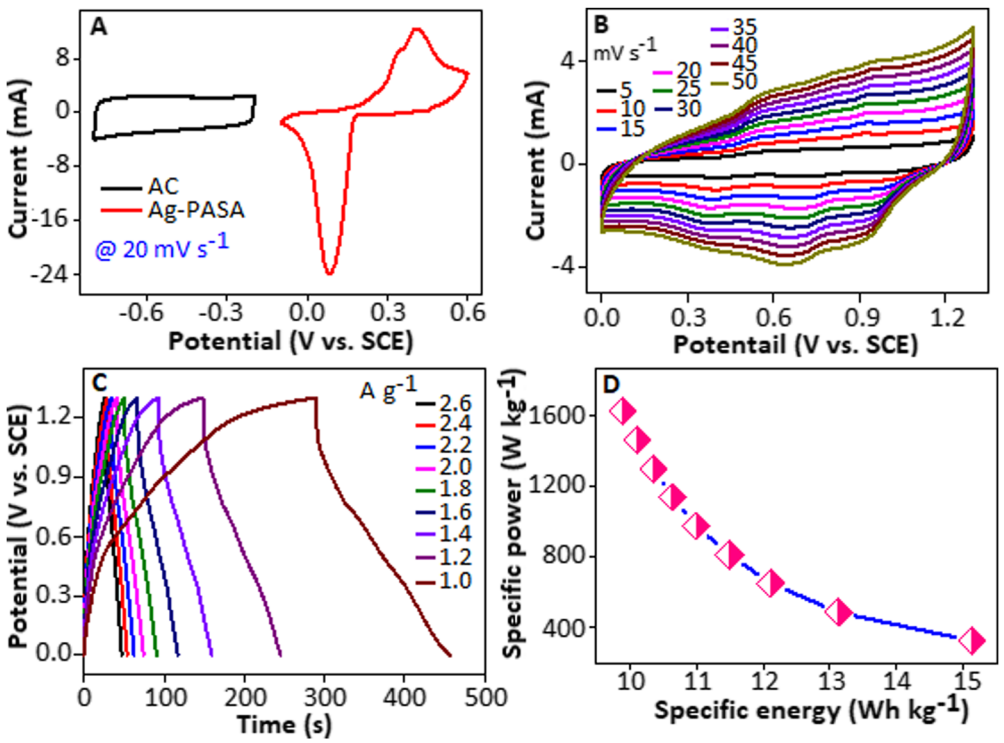

Fig. 8 (A) Comparative cyclic voltammograms of activated carbon and Ag-poly-aminosalicylic acid at 20 mV s^{-1} in a three-electrode setup. (B) Cyclic voltammetry curves of the asymmetric cell under various scan rates in the range of 5–50 mV s^{-1}. (C) Galvanostatic charge discharge curves of the cell under a specific current ranging from 1.0 to 2.6 A g^{-1}. (D) Ragone plot of the fabricated cell.

and reference electrodes; charge transfer resistance (R_{ct}), which reflects the resistance to charge transfer between the electrode and electrolyte; Warburg impedance (Z_w), which accounts for the resistance to ion diffusion in the electrolyte; pseudocapacitance (C_P), which is associated with faradaic redox reactions where charge storage occurs through electron transfer at the electrode surface and double layer capacitance (C_{dl}), arising from the electric double layer developed at the electrode–electrolyte interface.[55] The semicircle signifies the resistance linked to the faradaic reaction with the solution resistance (R_s) and charge transfer resistance (R_{ct}) values of 0.64 and 1.3 Ω, respectively. The appearance of the Warburg element (Z_w) in the circuit further confirms the predominance of the diffusion-controlled process in the redox reaction,[56] which can be proved as follows. Faradaic impedance ($Z_F(\omega)$) is expressed as the sum of the charge transfer resistance (R_{ct}) and the diffusion-controlled process ($Z_w(\omega)$), $Z_F(\omega) = R_{ct} + Z_w(\omega)$. As $\omega \rightarrow \infty$, the charge transfer process dominates the electrochemical performance, corresponding to the quasi-semicircle, observed in the high-frequency region, while for $\omega \rightarrow 0$, the electrochemical behaviour shifts to a diffusion-controlled process, which is evident by a linear response (45° inclined to Z') in the low-frequency region of the Nyquist plot. Mathematically, it can be represented as follows: $Z_w(\omega) = \sigma/\omega^{\alpha}\ (1 - j)$ or $\log|Z''| = \log\sigma + \alpha\log(1/\omega)$, where σ, j, ω and α represents Warburg coefficient, imaginary factor, angular frequency and transfer coefficient, respectively. The transfer coefficient (α) is determined from the slope of the linear plot of $\log|Z''|$ *versus* $\log(1/\omega)$, reflecting the electrochemical behaviour of the electrode material (α = 0.5 for Warburg behaviour).[43] The plot of $\log|Z''|$ *versus* $\log(1/\omega)$ for the electrode, displayed in Fig. 7C, with the slope value α = 0.52, suggests Warburg behaviour. A α value closer to 0.5 indicates diffusion-controlled energy storage, which is consistent with our cyclic voltammetry data. Furthermore, the diffusion coefficient of OH^- ions is estimated using the following equation: $D = R^2T^2/2A^2n^2F^2C^2{\sigma_\omega}^2$, where D, R, T, A, n, F, C and σ_ω represent diffusion coefficient, gas constant, temperature, surface area, number of electrons transfer, faradaic constant, concentration of OH^- ions and Warburg coefficient, respectively.[57] The value of σ_ω was derived from the slope of the linear plot of Z' *versus* $\omega^{-1/2}$, as illustrated in Fig. 7D. The calculated diffusion coefficient value was obtained as 1.55 × 10^{-16} $cm^2\ s^{-1}$. Impedance analysis concludes that the Ag-PASA composite electrode offers low charge transfer resistance and a high diffusion coefficient, which enhance the electrochemical reaction kinetics, thereby resulting in superior supercapacitor performance.

Two-electrode system: asymmetric supercapacitor

To illustrate the real-life application, an asymmetric supercapacitor was constructed using activated carbon as the anode electrode and Ag-PASA as the cathode electrode. The mass ratio of the electrode materials was calculated using mass balance eqn (S3) (ESI,† Section S2). Fig. 8A shows the cyclic voltammetry curves of activated carbon (−0.8 to −0.2 V) and Ag-PASA (−0.1 to 0.6 V) at 20 mV s^{-1} for a three-electrode setup. The calculated mass ratio was obtained as 0.3 and was determined using the specific capacity values 230 C g^{-1} for Ag-PASA and 76 C g^{-1} for activated carbon at 20 mV s^{-1}. The charge storage behaviour of the cell was performed at an operating voltage of 1.3 V. The quasi-rectangular cyclic voltammograms (Fig. 8B) of the cell revealed a redox behaviour, suggesting that the energy storage was governed by faradaic reactions with S_{CP} values of 55 and 18 C g^{-1} at 5 and 50 mV s^{-1}, respectively. The pattern of the galvanostatic charge–discharge curves (Fig. 8C) of the cell also confirms a faradaic process with S_{CP} values of 65 and 42 C g^{-1} at 1.0 and 2.6 A g^{-1}, respectively. At higher specific currents, the ability of electrolyte ions to effectively reach and interact with the active regions of the electrode was hindered. This limitation in ion transport led to a reduction in the S_{CP} values. Specific energy and power are calculated using eqn (S4) and (S5) (ESI†) and displayed as a Ragone plot in Fig. 8D.

The calculated specific energy values are 9 and 15 W h kg^{-1} at specific powers of 1625 and 325 W kg^{-1}, respectively, indicating an excellent electrochemical response. The electrochemical impedance spectrum of the cell and the magnified image of the spectrum are illustrated in Fig. 9A, main panel,

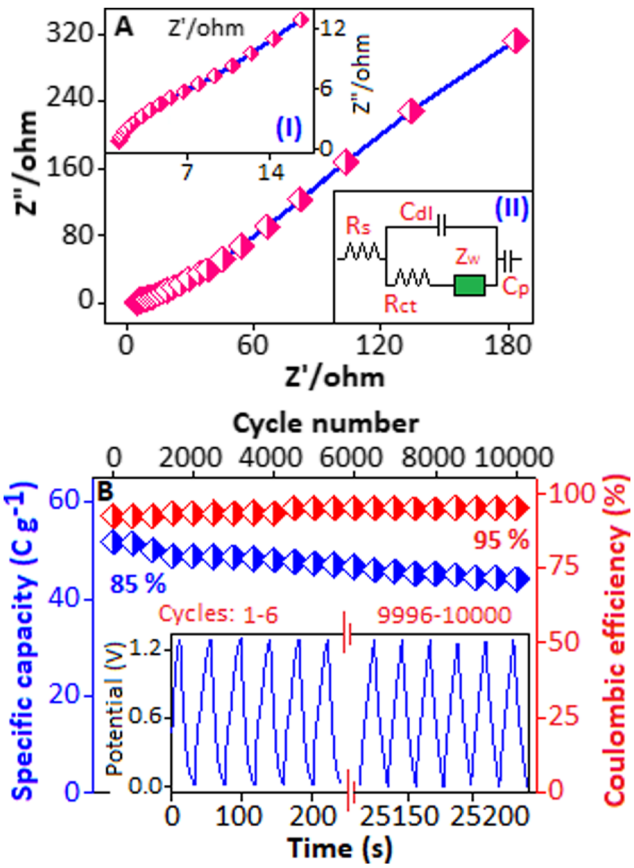

Fig. 9 (A) Nyquist plot of the cell. Inset figure (I) shows the magnified image of the Nyquist plot for the high-frequency region and inset figure (II) represents the equivalent circuit model. (B) Capacity retention and coulombic efficiency of the cell at 1.4 A g^{-1} for 10^4 cycles; the inset figure displays the first and last six charge–discharge cycles.

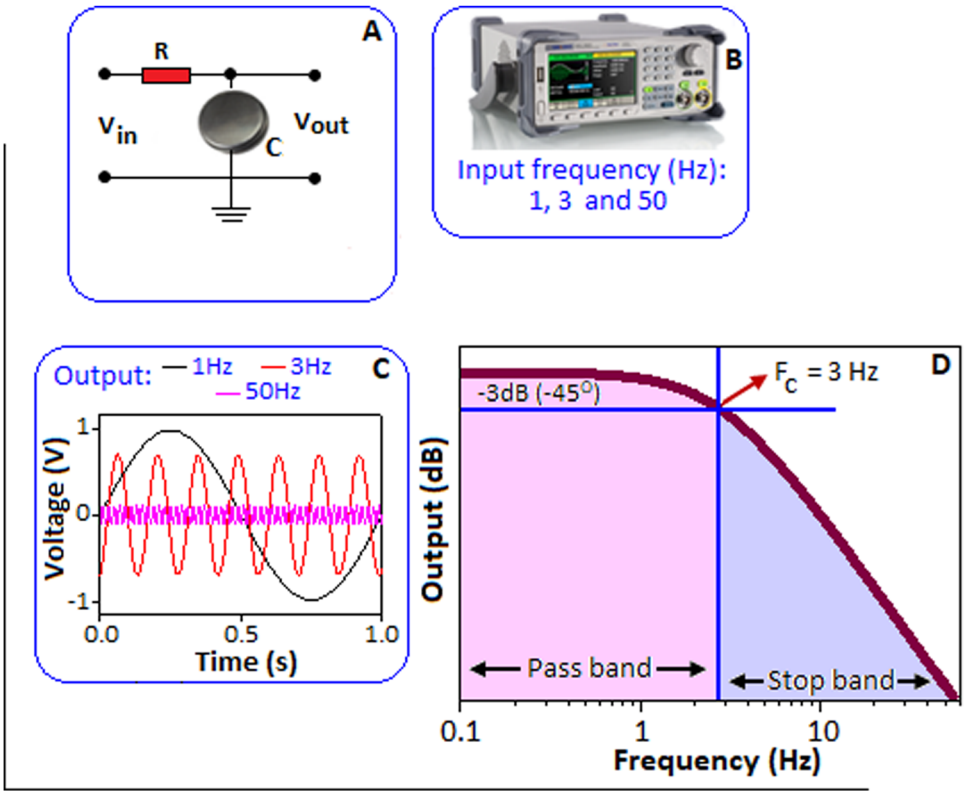

Fig. 10 (A) and (B) Experimental setup for low-pass filter application. Graphical representation of the extracted (C) experimental and (D) simulated results.

and Fig. 9A, inset (I), respectively. The fitted circuit model extracted from the Nyquist plot consists of a solution resistance (R_s) of 1.2 Ω in series with a charge transfer resistance (R_{ct}) of 4.9 Ω, along with a Warburg element (Z_w) and a double layer capacitance (C_{dl}), where R_{cts} is in parallel with C_{dl}. Additionally, the durability study of the cell was performed for 10^4 charge–discharge cycles at 1.4 A g^{-1} (Fig. 9B). The results revealed that the cell retained 85% of its original capacity and sustained a coulombic efficiency of 95% for the entire testing period. Fig. 9B, inset, displays the first and last six charge–discharge cycles.

Ag-poly-aminosalicylic acid-based supercapacitor for low pass filter application

Here, the fabricated supercapacitor device was applied for low pass filter application to attenuate high-frequency signals. Fig. 10A demonstrates the experimental setup for a low-pass filter circuit, which includes a resistor and a capacitor (laboratory made supercapacitor). In this setup, a sine wave input signal (V_{in}) with different frequencies (1, 3 and 50 Hz) was supplied using a function generator (GW Instek AFG-2225) (Fig. 10B). The output sine wave signal of the corresponding supplied frequencies was recorded using an oscilloscope (Tektronix TBS 1052B-EDU) (Fig. 10C). The circuit was simulated using LTspice software to estimate the theoretical values. Fig. 10D illustrates the frequency response when an AC signal with an amplitude of 1 V is applied to the circuit, varying in frequency from 0.1 to 50 Hz.

The cut-off frequency (f_c) of the low-pass filter was determined by the resistor (R) and capacitor (C) values in the circuit and calculated using the following formula: $f_c = \left(1/2\pi RC\right)$.[58] The filtered output signal (V_{out}) attenuates higher frequency components. The cut-off frequency, marked at 3 Hz in Fig. 10D, represents the point where the output amplitude drops to 70% of the input signal, corresponding to a −3 dB power drop. This defines the boundary between the passband (frequencies from 0.1 to 3 Hz) and the stopband (frequencies from 3 to 50 Hz). We also perform the experimental study by applying a similar kind of *RC* circuit, and the filter shows comparable results. Fig. 11 compares the input and output signals derived from both the experimental and simulated data. Fig. 11A and B show a 99% retention of output voltage at an input frequency of 1 Hz. Fig. 11C and D demonstrate a 70% output voltage retention at the cut-off frequency of 3 Hz. At a higher frequency of 50 Hz, the retention of output voltage decreases to 10%, as displayed in Fig. 11(E and F). These low-pass filters are widely used in various applications, including audio processing to eliminate high-frequency noise and in various power supplies to reduce ripples. In audio systems, it helps to improve sound quality by filtering out unwanted high-frequency interference and ensuring a cleaner and more accurate signal.

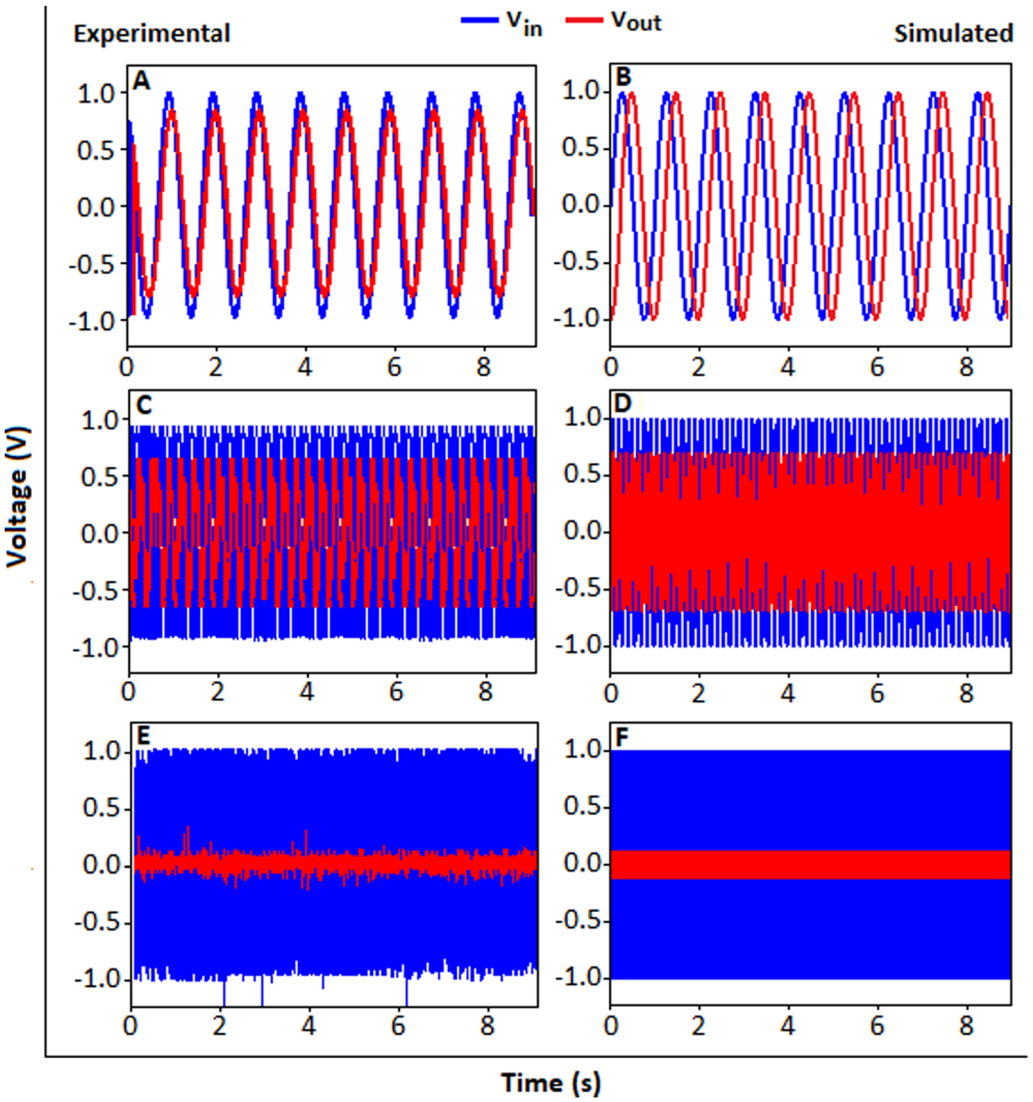

Fig. 11 Comparative input and output signals derived from both experimental and simulated data at ((A) and (B)) 1 Hz, ((C) and (D)) 3 Hz and ((E) and (F)) 50 Hz.

Similarly, in power supplies, low-pass filters are essential for smoothing out voltage fluctuations and reducing electromagnetic interference, which can influence the performance of electronic devices.[59]

Conclusion

In this work, a UV-light-mediated synthesis route was employed to fabricate a silver-polymer hybrid system aimed at developing a high-performance supercapacitor cathode electrode. This innovative approach leverages the energy of UV light to facilitate the reduction of silver ions, resulting in the formation of silver nanoparticles integrated within a polymer matrix. The integration of silver nanoparticles within a polymer matrix yielded impressive electrochemical properties, including a high specific capacity and excellent cycling stability. The use of Ag-PASA as a cathode material, alongside activated carbon as an anode, underlines its effectiveness in asymmetric supercapacitors. The promising performance of Ag-PASA as a supercapacitor, coupled with its ability to attenuate high-frequency signals, highlights its potential application in advanced energy storage and electronic filtering technologies.

Data availability

Data will be made available on request.

Conflicts of interest

The authors declare no competing financial interest.

Acknowledgements

This study was financially supported by the Faculty of Science, University Research Council and the Global Excellence and Stature program 4.0, University of Johannesburg.

References

1 Y. A. Sun, L. T. Chen, S. Y. Hsu, C. C. Hu and D. H. Tsai, *Langmuir*, 2019, **35**, 14203–14212.
2 N. Baig, I. Kammakakam and W. Falath, *Mater. Adv.*, 2021, **2**, 1821–1871.
3 X.-Y. Dong, Z.-W. Gao, K.-F. Yang, W.-Q. Zhang and L.-W. Xu, *Catal. Sci. Technol.*, 2015, **5**, 2554–2574.
4 C. Pattnaik, R. Mishra, A. K. Sahu, L. N. Sahoo, N. K. Sahoo, S. K. Tripathy and S. Sahoo, *Sens. Diagn.*, 2023, **2**, 647–656.
5 C. K. Tagad, S. R. Dugasani, R. Aiyer, S. Park, A. Kulkarni and S. Sabharwal, *Sens. Actuators, B*, 2013, **183**, 144–149.
6 S. Bose, R. Chatterjee, S. Roy and D. S. Bhadra, *J. Opt. Soc. Am. B*, 2016, **33**, 1014.
7 A. Meher, A. Tandi, S. Moharana, S. Chakroborty, S. S. Mohapatra, A. Mondal, S. Dey and P. Chandra, *Hybrid Adv.*, 2024, **6**, 100184.
8 V. Perla, S. Ghosh, P. Kumar, S. Ray and K. Mallick, *J. Mater. Sci.: Mater. Electron.*, 2019, **30**, 1–8.
9 P. Y. Jiang, Z. H. Xiao, Y. F. Wang, N. Li and Z. Q. Liu, *Bioelectrochemistry*, 2021, **138**, 107717.
10 Z. Luo, F. Li, C. Hu, L. Yin, D. Li, C. Ji, X. Zhuge, K. Zhang, K. Luo and L. Li, *J. Mater. Sci. Technol.*, 2020, **73**, 171–177.
11 A. Shamaeizadeh, F. Razi Astaraei and A. Kasaeian, *Results Opt.*, 2024, **14**, 100598.
12 M. Salve, A. Mandal, K. Amreen, P. K. Pattnaik and S. Goel, *Microchem. J.*, 2020, **157**, 104973.
13 W. Guo, W. Wei, H. Zhu, Y. Hu, H. Jiang and C. Li, *eScience*, 2023, **3**, 100082.
14 H. Yang, T. Xiong, Z. Zhu, R. Xiao, X. Yao, Y. Huang and M. S. Balogun, *Carbon Energy*, 2022, **4**, 820–832.
15 J. Li, T. Ouyang, L. Liu, S. Jiang, Y. Huang and M. S. Balogun, *J. Energy Chem.*, 2024, **93**, 368–376.
16 Z. Khanam, T. Xiong, F. Yang, H. Su, L. Luo, J. Li, M. Koroma, B. Zhou, M. Mushtaq, Y. Huang, T. Ouyang and M. S. Balogun, *Small*, 2024, **20**, 2311773.
17 S. Zhou, P. Huang, T. Xiong, F. Yang, H. Yang, Y. Huang, D. Li, J. Deng and M. S. Balogun, *Small*, 2021, **17**, 2100778.
18 X. Langa, L. Zhang, T. Fujita, Y. Ding and M. Chen, *J. Power Sources*, 2012, **197**, 325–329.
19 A. Abd-Elsalam, A. Selim, M. Tash, W. Khalifa and I. El Mahallawi, *Micro Nanostruct.*, 2024, **189**, 207821.
20 M. Sawangphruk, M. Suksomboon, K. Kongsupornsak, J. Khuntilo, P. Srimuk, Y. Sanguansak, P. Klunbud, P. Suktha and P. Chiochan, *J. Mater. Chem. A*, 2013, **1**, 9630–9636.
21 L. Tang, F. Duan and M. Chen, *J. Mater. Sci.: Mater. Electron.*, 2017, **28**, 1–9.
22 J. Singh and A. Dhaliwal, *Polym. Bull.*, 2024, **81**, 13155–13182.
23 D. Patil, S. Pawar, R. Devan, S. Mali, M. G. Gang, Y.-R. Ma, C. Hong, J. H. Kim and P. Patil, *J. Electroanal. Chem.*, 2014, **724**, 21–28.
24 J. Tian, D. Peng, X. Wu, W. Li, H. Deng and S. Liu, *Carbohydr. Polym.*, 2017, **156**, 19–25.
25 J. Ma, X.-Y. Tao, S.-X. Zhou, X.-Z. Song, G. Lin, W. Yao, Y.-B. Zhu, L.-T. Guo, Z.-S. Liu, H.-L. Fan and X.-Y. Wei, *J. Electroanal. Chem.*, 2019, **835**, 346–353.
26 I. Boyano, M. Bengoechea, I. de Meatza, O. Miguel, I. Cantero, E. Ochoteco, J. Rodríguez, M. Lira-Cantú and P. Gómez-Romero, *J. Power Sources*, 2007, **166**, 471–477.
27 P. Nie, Y. Zhao and H. Xu, *Ecotoxicol. Environ. Saf.*, 2023, **253**, 114636.
28 J. Jabłońska, K. Jankowski, M. Tomasik, D. Cykalewicz, P. Uznański, S. Całuch, M. Szybowicz, J. Zakrzewska and P. Mazurek, *SN Appl. Sci.*, 2021, **3**, 244.
29 S. Özkar and R. G. Finke, *J. Phys. Chem. C*, 2017, **121**, 27643–27654.
30 A. C. Dhayagude, A. Das, S. S. Joshi and S. Kapoor, *Colloids Surf., A*, 2018, **556**, 148–156.
31 K. Mallick, M. J. Witcomb and M. S. Scurrell, *J. Mater. Sci.*, 2004, **39**, 4459–4463.
32 M. Sastry, K. S. Mayya, V. Patil, D. V. Paranjape and S. G. Hegde, *J. Phys. Chem. B*, 1997, **101**, 4954–4958.
33 K. Mallick, M. Witcomb and M. Scurrell, *Mater. Chem. Phys.*, 2006, **97**, 283–287.
34 G. Magdy, E. Aboelkassim, S. Elhaleem and F. Belal, *Microchem. J.*, 2023, **196**, 109615.
35 M. Konkol, M. Kondracka, P. Kowalik, W. Próchniak, K. Michalska, A. Schwedt, C. Niewieszol and U. Englert, *Appl. Catal., B*, 2016, **190**, 85–92.
36 M. Tagowska, B. Pałys and K. Jackowska, *Synth. Met.*, 2004, **142**, 223–229.
37 K. Mallick, M. J. Witcomb and M. S. Scurrell, *J. Mater. Sci.*, 2006, **41**, 6189–6192.
38 M. Salvadori, R. Ando, C. Nascimento and B. Corrêa, *J. Environ. Sci. Health, Part A: Toxic/Hazard. Subst. Environ. Eng.*, 2017, **52**, 1–9.
39 M. P. Shilpa, S. J. Shetty, S. Surabhi, J.-R. Jeong, D. V. Morales, M. S. Murari, V. S. Bhat, S. R. Inamdar, Ravikirana and S. C. Gurumurthy, *J. Mater. Sci.: Mater. Electron.*, 2024, **35**, 860.
40 E. T. Kang, K. G. Neoh and K. L. Tan, *Prog. Polym. Sci.*, 1998, **23**, 277–324.
41 H. Luo, X. Ji and S. Cheng, *RSC. Adv.*, 2020, **10**, 8453–8459.
42 K. V. Sankar, Y. Seo, S. C. Lee, S. Liu, A. Kundu, C. Ray and S. C. Jun, *Electrochim. Acta*, 2018, **259**, 1037–1044.
43 J. J. William, S. Balakrishnan, M. Murugesan, M. Gopalan, A. J. Britten and M. Mkandawire, *Mater. Adv.*, 2022, **3**, 8288–8297.
44 J. Tian, Y. Xue, X. Yu, Y. Pei, H. Zhang and J. Wang, *RSC. Adv.*, 2018, **8**, 41740–41748.
45 M. Chandran, A. Thomas, A. Raveendran, M. Vinoba and M. Bhagiyalakshmi, *Solid State Sci.*, 2023, **139**, 107195.
46 A. A. Vannathan, T. Kella, D. Shee and S. S. Mal, *Ionics*, 2023, **29**, 4227–4241.
47 S. Dhibar and C. Das, *Ind. Eng. Chem. Res.*, 2014, **53**, 3495–3508.
48 D. S. Patil, J. S. Shaikh, S. A. Pawar, R. S. Devan, Y. R. Ma, A. V. Moholkar, J. H. Kim, R. S. Kalubarme, C. J. Park and P. S. Patil, *Phys. Chem. Chem. Phys.*, 2012, **14**, 11886–11895.
49 J. J. Benitto, J. J. Vijaya, B. Saravanakumar, H. Al-Lohedan and S. Bellucci, *RSC Adv.*, 2024, **14**, 8178–8187.
50 J. Johnson William, I. Manohara Babu and G. Muralidharan, *J. Chem. Eng.*, 2021, **422**, 130058.

51 K. Yang, K. Cho, D. S. Yoon and S. Kim, *Sci. Rep.*, 2017, **7**, 40163.
52 S. X. Wang, C. C. Jin and W. J. Qian, *J. Alloys Compd.*, 2014, **615**, 12–17.
53 D. R. Dar, S. Karna and A. Srivastava, *J. Power Sources*, 2015, **276**, 262–270.
54 A. Alam, G. Saeed and S. Lim, *Mater. Lett.*, 2020, **273**, 127933.
55 S. Nagamuthu and K. S. Ryu, *Sci. Rep.*, 2019, **9**, 4864.
56 D. Patil, S. Pawar, R. Devan, M. G. Gang, Y.-R. Ma, J. Kim and P. Patil, *Electrochim. Acta*, 2013, **105**, 569–577.
57 I. Shakir, Z. Almutairi and S. Saad Shar, *Ceram. Int.*, 2021, **47**, 1191–1198.
58 S. Niewiadomski, *Filter Handbook: A Practical Design Guide*, Heinemann Newnes, Oxford OX2 8EJ, 1989, ISBN: 0434-91378-2.
59 S. Pactitis, *Active Filters: Theory and Design*, CRC Press, Boca Raton, FL 33487-2742, 2018, ISBN: 978-1-4200-5477-4.